Chemical and physical erosion rhythms of the West African Cenozoic morphogenesis: The Ar-39-(40) Ar dating of supergene K-Mn oxides

Anicet Beauvais, Gilles Ruffet, Olivier Hénocque, Fabrice Colin

1

Chemical and physical erosion rhythms of the West African Cenozoic

morphogenesis: ^{39}Ar-^{40}Ar dating of supergene K-Mn oxides

4

Anicet Beauvais [a*], Gilles Ruffet [b], Olivier Hénocque [a], Fabrice Colin [c]

6

[a] *CEREGE (Centre Européen de Recherche et d'Enseignement de Géosciences de l'Environnement), Aix-Marseille Université, CNRS, IRD, CdF, BP 80, 13545 Aix-en-Provence Cedex 4, France*

10
11 [b] *Géosciences Rennes, Université de Rennes 1, CNRS, CAREN, 35042 Rennes Cedex, France*

12
13 [c] *IRD (Institut de Recherche pour le Développement), BP A5, 98848 Nouméa, Nouvelle-Calédonie*

15

16
17
18
19
20
21
22

23 [*]Corresponding author: beauvais@cerege.fr (Tel/Fax: 33 4 42 97 17 73/ 33 4 42 97 15 95)

24 **Abstract**

25

26   Chemical weathering and mechanical erosion are first order processes of long-term

27 tropical morphogenesis, which is still poorly deciphered for lack of time constraints. We

28 address this issue by laser-probe ^{39}Ar-^{40}Ar dating of generations of cryptomelane [$K_{1-2}Mn_8O_{16}$,

29 nH_2O] from the manganese ore deposit of Tambao in northern Burkina Faso. This

30 Mn deposit results from the supergene weathering of carbonate and silicate Mn-protores

31 underneath lateritic palaeolandsurfaces. It consists of an upper cryptomelane-rich domain, and

32 a lower domain where pyrolusite (β-MnO_2) is the dominant Mn-oxide. The oldest ^{39}Ar-^{40}Ar

33 ages (59-45 Ma) are obtained on surface outcrops while the youngest ones characterize deep

34 oxidation fronts (3.4-2.9 Ma). Apparent correlations of ^{39}Ar-^{40}Ar age groups with δ^{18}O and

35 eustatic curves allow definition of the different stages of morphogenesis. Paleocene-Eocene

36 ages (59-45 Ma), bracket a greenhouse period propitious to bauxitic weathering. The lack of

37 significant ages between ca. 45 Ma and 29 Ma characterizes a period dominated by

38 mechanical erosion, during which detrital sediments including lateritic materials were

39 accumulated in intracratonic basins allowing the exhumation of a new lateritic landsurface.

40 Two major weathering periods separated by a second erosion episode (24-18 Ma) are also

41 depicted at the end of Oligocene (29-24 Ma) and lower to mid-Miocene (18-11.5 Ma) in the

42 upper domain, during which newly shaped landsurfaces conspicuously weathered. The shorter

43 weathering and erosion episodes recorded in the lower domain from ca 18 Ma to ca 2.9 Ma

44 led to the final geomorphic changes that were conducive to the formation of glacis. The

45 preservation of old cryptomelane (59-45 Ma) in the upper part of the ore deposit indicates a

46 Cenozoic denudation limited to the erosion of previous bauxites, and partly, of ferricretes.

47

50

50   **1. Introduction**

51

52   Most lateritic deposits and tropical soils result from long-term meteoric weathering of the

53   lithosphere and are still widespread on the Earth surface, especially throughout the tropical

54   belt [*Pedro*, 1968; *Nahon*, 1991]. Following Gondwana break-up, physical and chemical

55   processes driven by epeirogeny and climate led to the development of tens of meters of thick

56   weathering mantles including bauxites and ferricretes, which are preserved on stepped relicts

57   of abandoned planation surfaces and pediplains [*Millot*, 1983; *Aleva*, 1984; *Bardossy and*

58   *Aleva*, 1990; *Nahon et al.*, 1992; *Tardy and Roquin*, 1998; *Chevillotte et al.*, 2006]. These

59   lateritic paleosurface relicts result from the combination of long-term weathering, incision

60   and erosion processes [*King*, 1967; *Partridge and Maud*, 1987]. According to the synthetic

61   morphogenetic sequence described in West Africa [*Vogt*, 1959; *Michel*, 1973; *Grandin*, 1976;

62   *Boulangé and Millot*, 1988; *Thomas*, 1994], the highest surfaces carrying bauxite dominate

63   landsurfaces with different generations of ferricrete (Figure 1). Manganese ore deposits may

64   also develop within specific rock's weathering mantles. Below the bauxitic paleosurface, the

65   intermediate ferricrete-capped relief dominates three pediments (Figure 1) so called lateritic

66   glacis in West Africa [*Thomas*, 1994], and defined as high, middle and low glacis. The term

67   glacis defines a gently inclined surface carrying detrital lateritic and bedrock materials.

68   The age determination of the paleosurfaces and their lateritic weathering remains a

69   critical issue in estimating the erosion rates and constraining the long-term tropical

70   morphogenesis and the evolution of continental palaeoclimates. A relative chronology of the

71   lateritic landsurfaces was assessed by examining the height differences between the

72   landsurfaces and the geochemical composition of the associated lateritic materials that

73   allowed a first estimation of the erosion rates [*Tardy and Roquin*, 1998]. However, better-

74   constrained ages of past chemical weathering and mechanical erosion periods can be obtained

75   by performing ^{39}Ar-^{40}Ar laser-probe dating of K-Mn oxides in supergene manganese ore

76 deposits that constitute a perfect alternative to the apatite fission track approach [*Gunnell*,

77 2003] to constrain the Cenozoic cratonic denudation for different time spans.

78   Previous geochronological studies proved the usefulness of K-Ar and ^{39}Ar-^{40}Ar methods

79 to date potassium-rich supergene minerals such as cryptomelane [*Vasconcelos et al*, 1992,

80 1994; *Lippolt and Hautmann*, 1995; *Ruffet et al.*, 1996; *Hénocque et al.*, 1998]. This K-Mn

81 oxide is believed to reflect strong lateritic weathering conditions [*Parc et al.*, 1989], and it is

82 ubiquitous in numerous supergene manganese ore deposits [*Nahon et al.*, 1984; *Beauvais et

83 al.*, 1987; *Roy*, 1981, 1988; *Dasgupta et al.*, 1992; *Ostwald*, 1992; *Pracejus and Bolton*, 1992;

84 *Varentsov*, 1996]. The Tambao Mn ore deposit in northern Burkina Faso is clearly integrated

85 in the continental scale geomorphological sequence (Figure 1) and its high cryptomelane

86 content [*Perseil and Grandin*, 1978] motivated ^{39}Ar-^{40}Ar geochronological investigations.

87 ^{39}Ar-^{40}Ar-laser method was first performed on two Mn-rich botryoidal concretions [*Henocque

88 et al.*, 1998] that showed an episode of cryptomelane formation between 44.5 and 50 Ma.

89 Later, ^{39}Ar-^{40}Ar age groups of 59-56 Ma, 47-44 Ma and 27-24 Ma were obtained on seven

90 samples of manganiferous pisolites deriving from a massive Mn-crust [*Colin et al.*, 2005].

91 These previous results allowed linking of the formation of surface Mn-crusts and pisolites to

92 the Paleogene bauxitic period. In this paper we investigate many more samples from drill

93 cores to better characterize the successive stages of the Mn-ore deposit formation that may

94 usefully document the long-term (Paleogene + Neogene) morphogenesis and denudation.

95

96 **2. Material, sampling and analytical methods**

97
98   Cryptomelane occurs in single or multiple generations associated with other Mn-oxides

99 [*Beauvais et al.*, 1987]. This is the K-rich end member of the hollandite Mn-oxide group with

100 a general formula, $A_{1-2}B_8O_{16}$, nH_2O (with A = K^+, Ba^{2+}, Na^+, Pb^{2+} and B = Mn^{4+}, Mn^{2+}, Fe^{3+},

101 Al^{3+}), and a tunnel structure made by double chains of MnO_6 octahedra [*Burns and Burns*,

102   1979; *Turner and Buseck*, 1979]. Large cations of the A site counterbalance the charge deficit

103   due to the Mn oxidation states and the other cations of the B site. The cryptomelane structure

104   increases its potassium and argon retentiveness, and thus its suitability for K-Ar and ^{39}Ar-^{40}Ar

105   geochronological investigations [*Vasconcelos et al.*, 1992, 1994].

106   The first applications of the K-Ar dating method to cryptomelane were very promising

107   despite problems of phase mixing and difficulties for extracting pure samples [*Chukhrov et*

108   *a*l., 1966; *Yashvili and Gukasyan*, 1974; *Varentsov and Golovin*, 1987; *Segev et al.*, 1991].

109   The small quantities required for ^{39}Ar-^{40}Ar-laser-probe dating reduce the mixing risks [*Ruffet*

110   *et al.*, 1996], which are further lessened by a precise sampling [*Hénocque et al.*, 1998].

111

112   **2.1. Petrography and mineralogy**

113

114   Samples were taken from drill cores DD2B, DDH76-02 and DDH76-09 of 110-meter and

115   40-meter-length, respectively (Figures 2 and 3) and from outcrops of manganese oxide

116   benches. DD2B, DDH76-02 and DDH76-09 cores were drilled on the high and low hills

117   (Figure 2). The altitude of samples in the cores and at the surface of the deposit is calculated

118   to allow comparisons and to define relations with landsurface processes.

119   Polished thin sections of samples were observed with an optical microscope (Leica DMRXP)

120   while scanning electron microscopy (SEM) was used for subsample investigations.

121   Manganese oxides were characterized by X-ray diffraction, using a Philips PW 1710

122   diffractometer with a Cu-tube anode (kα1 = 1.78896; kα2 = 1.79285) to avoid fluorescence

123   effects. Major chemical elements were measured out using ICP-OES.

124   When several cryptomelane generations occurred in a same sample, subsamples were

125   extracted and identified with a capital letter (BF96-327-A and BF96-327-B) or a two-digit

126   number (01, 02, 03, etc). The subsamples selected for ^{39}Ar-^{40}Ar dating were labeled with a

127   small letter added to the sample number (e.g., BF96-632-a1 and BF96-632-f2).

128

2.2. ^{39}Ar-^{40}Ar analysis

130

131   Samples selected for ^{39}Ar-^{40}Ar dating were hand picked from 0.5 mm thin slabs cut from

132   petrographic samples. They were wrapped in Al-foil to form small packets, which were

133   stacked into a column within which packets of flux monitors were inserted every 8 to 10

134   samples. This configuration allows determination of the vertical flux gradient with a precision

135   as low as ± 0.2%. Samples were irradiated in the 5C position of the McMaster reactor

136   (Hamilton, Canada) together with biotite monitor Bern4B (17.25 Ma) [*Hall et al.*, 1984], with

137   amphibole monitor Zartman Hb3gr (1072 Ma) [*Zartman*, 1964; *Turner*, 1971; *Roddick*,

138   1983], or with sanidine monitor Draz (24.99 Ma) [*Wijbrans*, pers. com.]. Because the sample

139   age was unknown, 4 to 70 hours irradiations were tested [*Hénocque et al.*, 1998], 25 hours

140   being the most suitable.

141   A VG$^{®}$ 3600 mass spectrometer equipped with a Daly$^{®}$ detector was used for analyses.

142   Each static measurement of argon isotopes corresponds to 11 peak hopping scans.

143   Backgrounds of the extraction and purification line were measured every first or third step

144   and subtracted from each argon isotope of the subsequent gas fractions. Typical blank values

145   were included in the ranges $3.2 \times 10^{-12} < M/e40 < 4.8 \times 10^{-13}$, $7.4 \times 10^{-14} < M/e39 < 4.6 \times 10^{-15}$, $6.6 \times 10^{-14} < M/e38 < 3.5 \times 10^{-16}$, $1.3 \times 10^{-13} < M/e37 < 1.7 \times 10^{-14}$ and $7.6 \times 10^{-14} < M/e36 < 2.1 \times 10^{-15}$ cm^3 STP. All

146

147   isotopic measurements were corrected for K, Ca and Cl isotopic interferences, mass

148   discrimination and atmospheric argon contaminations. Three consecutive steps accounting for

149   70% of the total ^{39}Ar released define a plateau age and the individual age fractions must agree

150   within 2σ error bars of the "integrated" age of the plateau segment. Pseudo-plateau ages can

151   be calculated, however, with less than 70% of the ^{39}Ar$_K$ released. All errors are quoted at the

152   1σ level and do not account for ^{40}Ar*/^{39}Ar$_K$ ratio and monitor age uncertainty, which is

153   included in the calculation of the plateau age error.

7

154

3. Geographical, geomorphological and geological setting

156
157   The Tambao Mn ore deposit is located in North Burkina Faso (14°47'N, 0°04'E) in the

158   sub-sahelian area close to a continental sedimentary basin (Figure 2). The mean annual

159   rainfall is 375 mm. The vegetation is composed of a grassy steppe alternating with forest

160   patches along river drainage axes. The Mn-ore deposit is composed of two hills

161   corresponding to lateritic landsurface relicts.

162

3.1. Distribution and characterization of lateritic landsurfaces

164
165   Four major landsurfaces are observed around Tambao (Figures 1 and 2). The highest one

166   is identified on the high hill between 353 and 325 meters elevation corresponding to a relict

167   of the intermediate landsurface [*Grandin*, 1976], which bears ferricrete and/or Fe-Mn and Mn

168   pisolitic crusts [*Colin et al.*, 2005]. The second landsurface observed between 325 and 300 m

169   on the highest hillslope corresponds to the high glacis, which is characterized by a quartzose

170   ferricrete incorporating reworked manganiferous and ferruginous pebbles originating from the

171   upper landsurface. The low hill also shows intermediate Fe-Mn crust relicts, the high glacis

172   being mainly represented between 325 and 300 m with a quartzose ferricrete (Figure 2). Two

173   lower landsurfaces are observed in the surrounding plain at about 300-280 m and < 280 m

174   corresponding to the middle- and low glacis, respectively. The former bears a ferricrete, while

175   the second is a sandy erosion surface.

176

3.2. Parent rocks and protores

178
179   Long-term lateritic weathering of a complex parent rocks assemblage has produced a 70

180   to 80 meter thick supergene manganese ore deposit (Figures 2 and 3). The Tambao Mn-

181 deposit hosts a reserve of about 15 Mt of manganese-ore with an MnO content of 75 wt.%

182 [*Boulanger and Sanguinetti*, 1970]. Four layers of manganese ores developed from weathered

183 Birimian (Paleoproterozoic age) metavolcanic and metasedimentary rocks (Figure 2),

184 composed of schist, micaschist, tuff, carbonate and quartzite [*Delfour*, 1963; *Grandin*, 1976].

185 Metamorphism of the Birimian rocks is related to syn- and post-tectonic granite and

186 granodiorite intrusions [*Picot and Trinquard*, 1969]. The metamorphic carbonates and tuffs

187 are the main protores of the Mn deposit reflecting the mining quality of the ore [*Boulanger*

188 *and Sanguinetti*, 1970; *Collins et al.*, 1971], which consists of a high grade carbonate ore with

189 hausmannite (Mn_3O_4), a rhodochrosite-rich carbonate ore and a low grade carbonate ore

190 containing kutnahorite ([Ca, Mg, Mn] CO_3). About 70% of the Mn ore derives from the

191 weathering of rhodochrosite (Figure 3) [*Picot and Trinquard*, 1969] and 30% from the

192 weathering of spessartine rich quartzite [*Perseil and Grandin*, 1978].

193

194 **4. Weathering and oxidation of protores**

195
196 **4.1. Petrography**

197
198   In drill core DD2B, at altitudes ranging from 241 and 265 m (Figure 3), the parent rock is

199 a very heterogeneous carbonate protore characterized by a ribbon pink carbonate matrix

200 embedding thin beds (0.1-1 m thick) of manganese oxides grains, which preserve the ribbon

201 structure. The transition between the protore and the oxidized Mn-ore is thin and partly

202 masked by a small albitite sill in drill DD-2B (Figure 3). Between 270 and 345 m (Figure 3),

203 the parent rock is directly replaced by the oxidized manganese ore (layer III), which also

204 partially preserves primary structures (folds and schistosity). The top of the core (345 m) is

205 mostly composed of detrital lateritic material. The drill core also cut across more or less

206 weathered granite and kaolinite-rich layers between 275 and 335 m (Figure 3). The oxidation

207 of the manganese carbonate protore induced a large porosity in which botryoidal manganese

208 oxide aggregates developed [*Hénocque et al.*, 1998].

209   The drill core DDH76-02 allows exploration of layers I, II and III (Figure 3). The parent

210 rock was not reached by the drill core but could be directly observed from outcrops.

211 Successions of manganese-rich and manganese-poor layers (10 cm thick) characterize the

212 quartzite formation. The manganese oxides layers deriving from the weathering of Mn-garnet

213 (spessartine) rich quartzite are thinner. Between 270 and 350 m, the manganese oxides

214 present various aspects, porous and light and/or massive and heavy with many botryoidal

215 concretions. In this core, manganese oxide layers alternate with weathered schist between 280

216 and 285 m, 300 and 310 m, and at 330 m, and with weathered granite between 315 and 325 m

217 and at 340 m, occurring as a quartz rich kaolinitic saprolite (Figure 3). The drill core DDH76-

218 09 allows investigation of layer IV, between 305 and 315 m, the lower part of the core being

219 composed of weathered schist between 290 and 305 m (Figure 3).

220

221 **4.2. Mineralogy and bulk chemistry**

222
223   Rhodochrosite ($MnCO_3$) and/or kutnahorite ($CaMn(CO_3)_2$) are the predominant primary

224 minerals of the carbonate protore, with small amounts of opaque minerals such as hausmanite

225 ($Mn^{2+}Mn^{3+}_2O_4$) and hetaerolite ($ZnMn_2O_4$), aligned parallel to the rock schistosity.

226 Transmitted light microscopy also reveals tephroite (Mn_2SiO_4) and rhodonite ($MnSiO_3$),

227 which are also oriented parallel to the rock schistosity. The weathering is characterized by *in*

228 *situ* transformation of rhodochrosite, hausmannite and tephroite into manganite ($MnOOH$),

229 todorokite ($[Mn^{2+}, Mg,Ca,Ba,Na,K]_2[Mn^{4+},Mn^{3+}]_7O_{12}. 3H_2O$), and pyrolusite ($\beta$-$MnO_2$), while

230 spessartine ($Mn_3Al_2[SiO_4]_3$) and rhodonite weathered into lithiophorite ($[Al,Li]MnO_2[OH]_2$).

231   The manganese oxide ore of layer II developed according to three stages. Spessartine was

232 replaced by lithiophorite. The voids resulting from the dissolution of quartz, kaolinite and

233 pyrolusite are filled with cryptocrystalline cryptomelane. The manganese oxides were

234 transformed into well-crystallized thin needles of cryptomelane (Figure 4).

235 The weathering of the carbonate protore leads to the formation of manganite, pyrolusite and

236 nsutite (γ-MnO$_2$) associated with todorokite. During a first weathering stage cryptomelane

237 occurs only in small veinlets (Figure 5a). Pyrolusite exhibits large prismatic crystals with a

238 characteristic fracture pattern. It is transformed into cryptomelane matrices in the upper part

239 of the deposit (Figure 5b) as indicated by the increase of K$_2$O (Figure 6). Multiple

240 cryptomelane generations also occur into botryoidal aggregates (Figure 5c).

241

242 **4.3. Potassium sources for cryptomelane**

243
244   Because the Mn-protores do not contain much potassium (Figure 6), sources of potassium

245 are found in the surrounding rocks of the basement and the metavolcanic and

246 metasedimentary rocks of the Birimian Supergroup (schists, granites, granodiorites and

247 migmatites). Large amounts of potassium can be also trapped with clay-organic molecules

248 and also into detrital minerals like illite and micas in the upper soil horizons. The release of

249 potassium in Mn^{2+}-rich solutions during the weathering of K-phyllosilicates into kaolinite can

250 contribute to the formation of cryptomelane [*Parc et al.*, 1989]. The depletion of Mn and K

251 from the upper part of the deposit was also observed during the late transformation of the

252 massive Mn-crust into pisolitic formation, this process being contemporaneous of the major

253 Eocene bauxitic period [*Colin et al.*, 2005]. Bauxites in the tropics formed under humid

254 climate with a dense vegetation cover that suggests high amounts of organic acids in

255 solutions, which can dissolve K-phyllosilicates and previously formed Mn- and K-Mn oxides,

256 with the release of K and Mn contributing to new cryptomelane growth in oxygenated zones

257 of the deposit.

258

259 **5. Geochronological investigation**

260
261 **5.1. ^{39}Ar-^{40}Ar age spectra configurations**

262
263   The stability of the K-Ar isotopic system within cryptomelane structure mainly depends

264 on geochemical interactions with fluids. The retentivity of argon and potassium isotopes in

265 cryptomelane has been investigated [*Lippolt et Hautmann*, 1995; *Vasconcelos et al.*, 1995;

266 *Vasconcelos*, 1999]. The various configurations of the age spectra obtained during ^{39}Ar-^{40}Ar

267 analyses have been discussed [*Vasconcelos et al.*, 1995; *Ruffet et al.*, 1996; *Hénocque et al.*,

268 1998; *Hautmann et Lippolt*, 2000] that allowed definition of three types of age spectra

269 improving the ^{39}Ar-^{40}Ar data interpretations.

270 Type 1 "staircase" age spectra are characterized by a rapid increase of the ages in the low

271 temperature steps followed by a rather flat segment that allows definition of a plateau age

272 (Figure 7a). These age spectra however suggest ^{40}Ar* losses linked to a younger weathering

273 "episode" that could have altered the peripheral intra crystalline retention sites or induced

274 secondary growth.

275 Type 2 "hump-shape" age spectra often show concordant "young" ages in the low and high

276 temperature steps and "old" ages in the intermediate degassing temperatures (Figure 7b)

277 indicating mixing of different manganese oxide generations. The low and high temperature

278 ages are maximum estimates of the youngest generation true age, whereas the intermediate

279 temperature ages are underestimates of the oldest generation true age.

280 Type 3 age spectra exhibit an irregular shape with a "staircase" in the low temperature steps,

281 the ages reaching a "maximum" followed by a decrease in the second part of the spectra up to

282 the fusion of the mineral (Figure 7c). Mixing of different mineral generations or ^{39}Ar recoil

283 during irradiation complicate the interpretation of these age spectra [*Turner and Cadogan*,

284 1974], although apparently significant ages can be often obtained.

285

5.2. ^{39}Ar-^{40}Ar results

287
288   The results were subdivided into three groups according to the altitude of the

289 cryptomelane samples (Figures 8, 9, and 10). ^{39}Ar-^{40}Ar runs are available as an online dataset.

290

291 5.2.1. First group of age spectra

292
293   The first group of age spectra corresponds to cryptomelane samples taken between the

294 groundsurface and -17 m depth, i.e., between altitudes of 342 to 325 m that are included

295 within the topographic boundaries of the intermediate landsurface (Figures 2 and 3). Fourteen

296 age spectra obtained on ten samples exhibit 4 Type 1 (staircase) and 9 Type 2 (hump) shapes

297 (Figure 8). The oldest apparent ages (≥ 43 Ma) are obtained for outcrops samples Col3 and

298 BF96-190 (Figure 8a). Col3 was taken from outcropping layer III, at an altitude of 325 m, on

299 the northeastern slopes of the high hill. This sample is part of a cryptomelane vein crossing a

300 pyrolusite ore, similar to the ones developed at the transition between pyrolusite- and

301 cryptomelane domains in the drill core DD2B (Figure 6). BF96-190 corresponds to the

302 transition (at an altitude of 345 m) between the massive ore (Layer III) and the pisolitic crusts

303 [*Colin et al.*, 2005] and it is the oldest one with a pseudo plateau age at 59.0 ± 0.1 Ma (45.2%

304 ^{39}Ar released). The age spectrum however exhibits a staircase shape with low temperature

305 apparent ages at ca 46.5 Ma indicating apparent ^{40}Ar* loss due to peripheral perturbations

306 and/or growth of a younger cryptomelane generation.

307   The four sub-samples of Col3 (b to e) are characterized by hump-shaped age spectra

308 (Figure 8a). Col3b and Col3e show the oldest pseudo plateau ages at 48.9 ± 0.1 Ma and 49.9

309 ± 0.2 Ma, respectively. Col3c shows a pseudo-plateau age at 44.9 ± 0.3 Ma, and Col3d is

310 characterized by an apparent age at 46.3 ± 0.2 Ma (58% ^{39}Ar released). The spectra show

311 "maximum ages" as young as the magnitude of the hump is high that could indicate a mixing

312 of two cryptomelane generations. The ages (ca. 45-50 Ma) for Col3 are however concordant

313 with the ones previously obtained for two cryptomelane concretions [*Hénocque et al.*, 1998].

314   Drill core samples yield systematically younger ages than outcrop and surface samples

315 (Figures 8b and 8c). Samples BF96-202c3, 211, 215 and 218-a of the upper part of drill core

316 DDH-76-02 (342-330 m) are characterized by hump shaped age spectra with maximum

317 apparent ages between 34-40 Ma in the intermediate temperature steps (Figure 8b). BF96-

318 218a and 215 exhibit small concordant pseudo-plateau ages in the low temperature steps at

319 24.6 ± 0.8 Ma and 24.1 ± 1.2 Ma, respectively (Figure 8b). BF96-229 is a small cryptomelane

320 vein in the weathered granite between layers II and III in drill core DDH-76-02 (326 m) and it

321 displays a plateau age at 17.8 ± 0.1 Ma with 64.1% ^{39}Ar released (Figure 8b). The staircase

322 age spectrum of sample BF96-104 (327 m in Drill core DD2B) also allows definition of a

323 plateau age at 17.4 ± 0.2 Ma with 87% ^{39}Ar released (Figure 8c). Age spectra of samples

324 BF96-107 and BF96-108a (upper part of drill core DD-2B) display "old" and "young"

325 apparent ages in the low to intermediate temperature steps at 25.6 ± 0.4 Ma (20% of the total

326 ^{39}Ar released) and 17.7 ± 0.4 Ma (23% of the total ^{39}Ar released), respectively, which are

327 nearly concordant with the fusion step apparent age (Figure 8c). The age-frequency diagram

328 (Figure 8d) reveals three major age intervals, 35-50, 23-27 and 15-18 Ma.

329

330 5.2.2. Second group of age spectra

331
332   The second group of age spectra consists of samples taken at depths ranging from -18 to -

333 42 m that correspond to the lower part of the cryptomelane domain at altitudes of 324 to 300

334 m (Figure 3), i.e., the topographic boundaries of the high glacis landsurface (Figure 2). This

335 group of 19 samples (Figure 9) shows 24 age spectra with 6 Type 1 (staircase) shapes, 17

336 Type 2 (hump) shapes, and 1 Type 3 shape (BF96-101-b2). Samples of the high hill cores

337 (DD2B and DDH76-02) were taken within the layer III between 325 and 320 m (BF96-97,

338 98, 101 and 102) and between 315 and 300 m (BF96-251, 256, 96, 260, 94 and 273). Samples

339 of the low hill core were taken between 315 and 313 m (BF96-559, 561 and 563) and between

340 309 and 300 m (BF96-571-02, 575-b and 577) (Figure 3). Sample Col1 and BF93-632-f2 are

341 outcrop and surface sample, at altitudes of 320 m and 307 m, respectively.

342   Col1 is cryptomelane developing from metasomatism of pyrolusite (Figure 5b). Col1

343 duplicates irradiated for 5 and 70 hours yielded very similar hump shape age spectra (Figure

344 9a) indicating no ^{39}Ar recoil during irradiation. The two age spectra show nearly concordant

345 maximum ages in the range 45.3 ± 0.4 - 44.4 ± 0.1 Ma while one obviously shows a small

346 pseudo-plateau age at 27.3 ± 0.7 Ma derived from six concordant steps at low temperature (5

347 to 15% of the total ^{39}Ar released) that is also concordant with high temperature ages (Figure

348 9a). BF93-632 is a hollandite concretion sampled underneath the high glacis ferricrete at an

349 altitude of 307 m. A sub-sample (BF96-632-a1) yields an interesting hump-shaped age

350 spectrum with concordant low and high temperature ages at ca 16 Ma (Figure 9a). A second

351 sub-sample (BF96-632-f2) is characterized by a staircase age spectrum with low temperature

352 ages at ca. 16 Ma (Figure 9a), and an intermediate to high temperature pseudo-plateau age at

353 36.2 ± 0.2 Ma (46.3% of the total ^{39}Ar released).

354 Samples of DD2B core are characterized by plateau ages calculated from staircase and hump-

355 shaped age spectra around 24 Ma (Figures 9b) and at 14.9 ± 0.1 Ma and 17.1 ± 0.1 Ma

356 (Figure 9c). An older plateau age was also calculated at 28.8 ± 0.1 Ma (BF96-251) while four

357 younger plateau ages are evident between 11.5 ± 0.2 Ma and 14.6 ± 0.3 Ma for DD76-02 core

358 samples (Figure 9d). Sample BF96-260 with younger apparent ages (ca 21-22Ma) exhibits a

359 clear hump shape that does not allow plateau age calculation (Figure 9d).

360 Samples of DDH76-09 core provided plateau ages at 27.1 ± 0.3 Ma, and two younger at ca.

361 24-25 Ma (Figure 9e). One sample (BF96-577) at an altitude of 304 m is characterized by a

362   unique "older" age at 36.3 Ma (Figure 9f) that is comparable with the intermediate to high

363   temperature age of BF96-632-f2 (Figure 8a). The age frequency diagram reveals four age

364   and/or age intervals, 12.5, 14-17, 21-25 and 27-29 Ma (Figure 9g) all being concordant with

365   objectively calculated pseudo-plateau and plateau ages.

366

367   5.2.3. Third group of age spectra

368
369   The third group of age spectra consists of samples mainly taken from the pyrolusite-rich

370   core (BF96-62, 91, 93, 299, 314, 318, 322, 327, 581, 653) between depths of -42 m to -89 m

371   corresponding to altitudes of 300 m to 253 m, which are also the topographic ranges of the

372   two lowest glacis (Figures 2 and 3). BF96-62 is a thin cryptomelane rim around a small

373   pyrolusite concretion in the carbonate protore of DD2B core. Sample BF96-653 is a fragment

374   of a cryptomelane vein crossing the exhumed schist saprolite of the low glacis. This third

375   group includes 11 age spectra with 5 staircase and 6 hump shapes that allowed the calculation

376   of 7 pseudo-plateau ages lower than 20 Ma (Figure 10).

377   Large error bars shown by some age spectra (BF96-62-03, BF96-91 and BF96-322)

378   characterize the very low K_2O content of these samples (e.g., 0.2 wt.% for BF96-91). Samples

379   BF96-93 and BF96-299 of the high hill cores display plateau ages at 11.5 ± 0.1 Ma and 18.3 ±

380   0.3 Ma, respectively (Figures 10a and 10b). The age spectrum of BF96-581 at 293 m altitude

381   yields older apparent ages at ca. 24 Ma, which are concordant with the plateau ages obtained

382   upper for samples BF96-561-02, 563-02 and 575-b (Figure 9e).

383   Three plateau ages were also calculated for samples BF96-653, BF96-314, BF96-318 at

384   5.8 ± 0.1 Ma, 6.5 ± 0.1 and 7.2 ± 0.1 Ma, respectively (Figures 10a and 10b). The hump

385   shaped age spectrum of BF96-318 exhibits concordant apparent ages at ca. 3.5-4 Ma in the

386   low and high temperatures. The youngest ages are displayed by three samples of DDH76-02

387   core close to the oxidation front in the pyrolusite domain. The apparent age at ca. 3 ± 1.3 Ma

388 measured for BF96-62-03 (Figure 10a) is concordant with plateau ages at 3.4 ± 0.1 Ma

389 (80.6% ^{39}Ar released) and 2.9 ± 0.1 Ma (74.7% ^{39}Ar released) yielded by samples BF96-327-

390 a1 and -327-a2, respectively (Figure 10b). Ages at 5.5-7.5 Ma and ca. 3 Ma are well depicted

391 by the age frequency diagram, which also reveals ages at 11.5, 18 and 22.5 Ma (Figure 10c).

392

393 **6. ^{39}Ar-^{40}Ar ages interpretation**

394

395 The oldest ages (ca. 59 Ma to ca. 45 Ma) obtained for cryptomelane of outcrop and

396 surface samples (Figure 8a) are coherent with the ages of massive Mn-crust and pisolites

397 [*Colin et al.*, 2005], and also the ages of botryoidal concretions [*Hénocque et al.*, 1998].

398 These ages indicate a sustained humid and warm paleoclimate for at least 14 Ma that could

399 represent the duration of the Eocene bauxite formation period. The age ca. 49 Ma obtained for

400 a cryptomelane at -25 m depth (Col 3) allows estimation of 2.5 m. Ma^{-1} for the oxidation front

401 sinking rate between 59 and 49 Ma. However, the staircase and hump shapes of age spectra of

402 drill core samples in the highest part of layers I, II and III suggests a reactivation of

403 geochemical weathering process, and thus a rejuvenation of older minerals (Figure 8).

404 Concentric banded overgrowth structures (e.g., botryoidal) effectively result from repeated

405 geochemical mobilizations of Mn and K that led to newly formed cryptomelane generations

406 (Figure 5c). Their crystal size is so small that handpicking sampling inevitably implied

407 mixings of "old" and "young" generations characterized by hump-shaped age spectra, with

408 maximum apparent ages in the range 40-33 Ma and lower than the plateau and pseudo-plateau

409 ages of outcrop samples (Figure 8a).

410 The age spectra of the first group document two subsequent weathering episodes (Figure

411 8d). An episode at ca 27-23 Ma is obviously defined in the upper part of the cryptomelane

412 domain as shown by the diagram of plateau and pseudoplateau ages *vs*. altitude where the

413 elevation ranges of each lateritic landsurface are also represented (Figure 11a). This episode

414 was also characterized in the pisolitic crust [*Colin et al.*, 2005], where it superimposed to the

415 lateritic episode at ca. 46 Ma. The lower part of the cryptomelane domain also yields

416 reproducible pseudo-plateau and plateau ages in the range 29-24 Ma (Figure 9) that could

417 document the downward propagation of the oxidation front at an average rate of 2 m. Ma^{-1}.

418 Another weathering episode is depicted by low temperature ages around 18-17 Ma (Figures

419 8b, 8c and 8d). Plateau ages at 18-17 Ma were also obtained in the lower part of the

420 cryptomelane domain and for vein cryptomelane of the upper pyrolusite domain (Figures 9c

421 and 10b) that further supports the likelihood of this weathering episode.

422 The youngest ages, ca. 18 to ca. 3 Ma, document active weathering and oxidation

423 processes during the Neogene. Cryptomelane often crystallized in small veins and concretions

424 in the pyrolusite rich lower parts of the deposit indicating episodic deep circulations of

425 weathering solutions. The cryptomelane crystals are characterized by plateau ages ranging

426 between 17.8 Ma and 2.9 Ma (Figure 10), and these ages are as young as samples collected

427 close to the oxidation front (Figure11a). Figure 11a also includes ^{39}Ar-^{40}Ar ages obtained by

428 previous studies [*Henocque et al.*, 1998; *Colin et al.*, 2005]. Figure 11b shows less apparent

429 age scattering and increasing purity of analyzed parageneses with depth.

430 Although the increasing diversity of ^{39}Ar-^{40}Ar ages from the bottom to the top of the Mn-

431 deposit (Figure 11b) suggests a continuous chemical weathering for 59 Ma, five main

432 weathering periods can be differentiated. The first from ca. 59 Ma to ca. 45 Ma characterizes

433 a long weathering period, during which bauxites formed all over the tropical belt [*Bardossy*

434 *and Aleva*, 1990]. The second occurred in the range 29-24 Ma with an occurrence at 21 Ma

435 (Figure 11a), and it was well depicted in the ore deposit (Figure 9). The intermediate

436 landsurface was also deeply weathered during this major period. The three last periods are

437 characterized by short weathering episodes, 18-11.5 Ma, 7.2 -5.8 Ma and 3.4-2.9 Ma (Figure

438   11a), during which the three glacis were probably weathered along with recurrences between

439   18-11.5 Ma in the pre-existing intermediate landsurface profile (Figure 11a).

440

441   **7. Lateritic weathering, palaeoclimates, long-term morphogenesis and denudation**

442

443   Petrographical and geochemical patterns of the different lateritic landsurfaces and the

444   height difference between the landsurfaces reflect differences in duration and intensity of

445   weathering and erosion processes linked to contrasted paleoclimates between the Palaeogene

446   and Neogene [*Tardy and Roquin*, 1998]. The comparison of the global $\delta^{18}O$ and eustatic

447   curves [*Miller et al.*, 2005] with ^{39}Ar-^{40}Ar ages distribution (Figures 12a, 12b and 12c) and

448   with the intracontinental sedimentary sequences (Figure 13a) contributes to a better

449   understanding of the influence of Cenozoic paleoclimatic changes on West African

450   landscapes. The age frequency histogram in Figure 12c incorporates all the results including

451   those obtained from the previous studies [*Henocque et al.*, 1998; *Colin et al.*, 2005]. The

452   series of ^{39}Ar-^{40}Ar ages and time intervals between these ages may document, as a surrogate

453   for long-term paleoclimatic proxies, the major chemical weathering (warm/humid climate)

454   and mechanical erosion (cold/dry climate) periods (Figures 12 and 13b). The altitude of dated

455   samples and the elevation (maximum) of each planation landsurface allow estimation of

456   average mechanical erosion rate for different time spans corresponding to the successive

457   lateritic planation cycles.

458   From Paleocene (ca. 60 Ma) to middle Lutetian (ca. 45 Ma), $\delta^{18}O$ is low and the eustatic

459   level is high [*Zachos et al.*, 2001; *Miller et al.*, 2005] (Figure 12a and 12b). The identification

460   of marine sediment incursions between the "Continental Intercalaire" and the basal

461   unconformity in the Iullemmeden basin, 150 km North North-East and East of Tambao

462   (Figure 13a) indicates a maximal extension of the Saharan sound between 55 and 60 Ma in

463   western Niger [*Petters*, 1977]. The marine sediments are mainly composed of carbonates,

464   marls, and clays dominated by sepiolite, palygorskite and attapulgite [*Millot*, 1970; *Chamley*

465   *et al.*, 1988; *Ly and Anglada*, 1991] that characterize biogeochemical sedimentation. This was

466   also linked to the genesis of thick bauxitic weathering mantles inland including a differential

467   sequestration of Fe and Mn according to their respective chemical mobility.

468   Bauxites have been described on Precambrian basement and also upon the unconformity

469   (Figure 13a) between the "Continental Intercalaire" deposits and the siderolithic "Continental

470   Terminal" (CT) in the Iullemmeden basin [*Faure*, 1966; *Gavaud*, 1977; *Lang et al.*, 1990].

471   The basal sequence of CT (Upper Lutetian) is characterized by ooliths, which are also

472   interstratified within the upper siderolithic sediments [*Boudouresque et al.*, 1982]. This

473   suggests that dissolved iron input originated from inland lateritic formations, whereas the

474   siderolithic detrital sediments corresponds to the mechanical erosion of lateritic weathering

475   mantles according to alternating humid and dry palaeoclimates, respectively. A ferricrete

476   specific of the intermediate surface has also been described upon the CT sediments (Figure

477   13a) of Mali and Niger [*Gavaud*, 1977; *Lang et al.*, 1990]. Relicts of a similar ferricrete are

478   also present on the high hill where ^{39}Ar-^{40}Ar ages of 59-45 Ma and also 29-24 Ma were

479   measured. The field observations and ^{39}Ar-^{40}Ar data imply that the bauxitic and intermediate

480   ferruginous paleolandsurfaces intersected near the Tambao Mn-deposit (Figure 13a), thus

481   questioning the supposed Pliocene age of the ferricrete upon the CT sediments [*Michel*, 1973;

482   *Grandin*, 1976; *Gavaud*, 1977].

483   Biogeochemical sedimentation ceased in mid-Eocene (Lutetian) as indicated by the

484   marine sedimentary gap at the bottom of Iullemmeden [*Faure*, 1966; *Boudouresque et al.*,

485   1982] and Senegalese basins [*Ly*, 1985]. This gap might be correlated to the sea level drop

486   between ca. 34 Ma and ca. 29 Ma [*Miller et al.*, 2005] (Figure 12b) that resulted from

487   Oligocene global cooling concomitant with the development of East Antarctic Ice Sheet

488   [*Salamy and Zachos*, 1999; *Zachos et al.*, 2001]. These changes have induced drier climatic

489   conditions on continents [*Lawver et al.*, 1992], with an apogee at ca 33.5 Ma [*Kennett and*

490   *Shackleton*, 1976; *Zachos et al.*, 1994, 1996; *Salamy and Zachos*, 1999; *Miller et al.*, 2005]

491   and a persistence until the Middle Oligocene-Early Miocene [*Flower and Kennett*, 1994] as

492   indicated by $\delta^{18}O$ increase [*Miller et al.*, 2005] (Figure12a). No significant ^{39}Ar-^{40}Ar ages

493   were obtained in the range 45-29 Ma (Figure 12c). Following the eustatic change, the

494   progressive sea retreat towards north and south [*Faure*, 1966] led to the incision and erosion

495   of previous lateritic landforms. An average mechanical erosion rate of 3 m. Ma^{-1} can be

496   calculated for the period 45-29 Ma assuming an elevation of 400 m for the warped bauxitic

497   landsurface, and the intermediate surface at 350 m (Figure 13a). At that time, continental

498   sedimentation (siderolithic CT) could include lateritic materials eroded from early bauxitic

499   and clay-ferruginous weathering mantles. The bauxite erosion allowed the exhumation of

500   ferruginous materials, i.e., the formation of the ferricrete-bearing intermediate landsurface.

501   The next major episode of chemical weathering in Tambao occurred around 29-24 Ma

502   (Figure 12c) corresponding with late Oligocene global warming [*Zachos et al.*, 2001] and to a

503   relative stability of the global sea level [*Miller et al.*, 2005]. This age interval was particularly

504   well represented in the Mn-ore deposit (Figure 9b) and could date the weathering of the

505   recently exhumed intermediate lateritic profiles (Figures 11a and 13b) and also the formation

506   of the older ferricrete observed upon the Iullemmeden CT sediments (Figure 13a).

507   Although Milankowitch glacial-interglacial cycles are well documented in the Oligocene

508   [Retallack et al., 2004], the global Earth climate was frankly driven by a glacial-interglacial

509   dynamic from the boundary Oligocene/Miocene [*Zachos et al.*, 2001]. The three ferruginous

510   glacis could be formed between 24 and 3 Ma as results of the alternation of mechanical

511   erosion and chemical weathering episodes (Figures 12 and 13b) according to low frequency

512   climatic oscillations but higher seasonality. Except an age at ca 21 Ma, the interval 24-18 Ma

513   could have been propitious to the mechanical erosion of the intermediate landsurface at an

514 average rate of 4 m. Ma^{-1}, at least partially, and to the final denudation of bauxitic remnants.

515 This major mechanical erosion episode led to the setting of the high glacis, which was

516 weathered at 18-17 Ma, 15-14.5 Ma and 12.7-11.5 Ma (Figures 11a, 12c and 13b) as

517 suggested by the increase of δ^{18}O and the relatively high sea level [*Berger and Wefer*, 1996;

518 *Miller et al.*, 2005] (Figures 12a and 12b). Coarser lateritic materials including bauxite and

519 ferricrete debris were also reworked into the newly formed high glacis landsurface that is

520 characteristic of glacis-forming processes under drier climatic conditions [*Vogt*, 1959; *Michel*,

521 1973, 1978; *Grandin*, 1976; *Boulangé and Millot*, 1988; *Thomas*, 1994]. Notice also that the

522 weathering of intermediate surface remnants could have been reactivated between 18 and 11.5

523 Ma (Figure 11a) confirming observations in other West African areas [*Beauvais et al.*, 1999,

524 2004]. The interval 11.5-7.2 Ma would correspond to the mechanical erosion of the high

525 glacis at an average rate of 6 m. Ma^{-1} leading to the middle glacis emplacement before it's

526 weathering at 7.2-5.8 Ma. A short erosive episode from ca. 5.8 to 3.4 Ma at an average rate of

527 8 m. Ma^{-1}, which is comparable with the previously estimated erosion rate using cosmogenic

528 nuclides [*Brown et al.*, 1994], allowed emplacement of the low glacis, before this latter was

529 weathered at ca 3.4-2.9 Ma (Figure 13b).

530

531 **8. Conclusion**

532
533 ^{39}Ar-^{40}Ar ages were obtained on different cryptomelane generations sampled on outcrops

534 and drill cores in the Mn-ore deposit of Tambao (North Burkina Faso), which mainly

535 developed from the oxidation of carbonate and silicate protores. The ^{39}Ar-^{40}Ar ages were

536 compared with the variations of the global δ^{18}O and eustatic curves that documented

537 successive Cenozoic chemical weathering and mechanical erosion periods driven by the

538 alternation of warm/humid climates and cold/dry climates, respectively. The interval 59-45

539 Ma corresponds to the Eocene bauxitic period, implying that cryptomelane formed during

540 warm and humid periods in well-oxygenated lateritic weathering profiles. However, bauxite

541 ferruginization and thus the starting of ferricrete individualization in the profiles characterized

542 the end of this period, ca. 50 to ca. 45 Ma. The lack of significant measured ages from ca. 45

543 Ma to ca. 29 Ma corresponds to a period dominated by incision and erosion processes under

544 drier climatic conditions, during which continental sediments started to accumulate in West

545 African intracratonic basins. The intermediate landsurface was probably formed at the end of

546 this period (ca. 34 to ca. 29 Ma). Then the newly exposed lateritic landsurface was further

547 weathered between 29 and 24 Ma. This age interval could also date the ferricrete upon

548 Iullemmeden CT sediments. The high glacis could have been shaped in the interval of 24-18

549 Ma, weathered around 18-17, 15-14 and 12.7-11.5 Ma, and eroded between 11.5 and 7.2 Ma,

550 an interval propitious to the settlement of the middle glacis before this one was weathered at

551 7.2-5.8. The lowest glacis was shaped in the interval 5.8-3.4 Ma before the last short chemical

552 weathering episode at 3.4-2.9 Ma. Our results allow average estimations of the oxidation front

553 sinking rate of 2.5 m. Ma^{-1} for the period 59-45 Ma against 1.5 m. Ma^{-1} for the period 59-3

554 Ma. The average erosion rates of the successive lateritic landsurfaces would be 3 to 8 m. Ma^{-1}

555 for the period 59-3 Ma. However, persistence of lateritic landsurface relicts in the landscape,

556 and old cryptomelane (59-45 Ma) in the upper part of the ore deposit, indicates low Cenozoic

557 denudation rates, of the order of the height differences between the lateritic landsurfaces.

558

563

References

Aleva, G.J.J. (1984), Lateritisation, bauxitisation and cyclic landscape development in the Guiana shield, in *Bauxite*, proceedings 1984 bauxite symposium, edited by L. Jacob Jr., pp. 111-151, AIME, New York.

Bardossy, G., and G.J.J. Aleva (1990), *Lateritic bauxites*, Elsevier, Amsterdam.

Beauvais, A., A. Melfi, D. Nahon, and J.J. Trescases (1987), Pétrologie du gisement latéritique manganésifère d'Azul (Brésil), *Miner. Deposita*, *22*, 124-134.

Beauvais A., M. Ritz, J-C. Parisot, M. Dukhan, and C. Bantsimba (1999), Analysis of poorly stratified lateritic terrains overlying a granitic bedrock in West Africa, using 2D electrical resistivity tomography, *Earth Planet. Sci. Letters*, *173*, 413–424.

Beauvais A., M. Ritz, J-C. Parisot, C. Bantsimba, and M. Dukhan (2004), Combined ERT and GPR methods for investigating two stepped lateritic weathering systems, *Geoderma*, *119*, 121-132.

Berger, W.H., and G. Wefer (1996), Expeditions into the past: Paleoceanographic studies in the south Atlantic, in *The south Atlantic: present and past circulation*, edited by G. Wefer et al., Springer editions.

Boudouresque, L., D. Dubois, J. Lang, and J. Trichet (1982), Contribution to the stratigraphy and paleogeography of the western edge of the Iullemmeden basin during the upper Cretaceous and Cenozoic (Niger and Mali – West Africa), *Bull. Soc. Géol. France*, *24*, 685-695.

Boulangé, B., and G. Millot (1988), La distribution des bauxites sur le craton Ouest Africain, *Sci. Géol. Bulletin*, *41*, 113-123.

Boulanger, J.J., and H. Sanguinetti (1970), Evaluation générale du gisement de manganèse de Tambao. Haute Volta, Enquêtes sur le développement minier dans le nord-est et facteurs associés de transport, *Rapport n°3*, 48 pp., PNUD, Ouagadougou, Burkina Faso.

589 Brown, T.E., D.L. Bourlès, F. Colin, Z. Sanfo, G.M. Raisbeck, and F. Yiou (1994), the

590 development of iron crust lateritic systems in Burkina Faso, West Africa examined with in-

591 situ-produced cosmogenic nuclides, *Earth Planet. Sci. Letters*, *124*, 19-33.

592 Burns, R.G., and V.M. Burns (1979), Manganese oxides, in *Marine minerals*, edited by P.H.

593 Ribbe, pp. 1-46, Mineral. Soc. Am., Washington DC.

594 Chamley, H., P. Debrabant, and R. Flicoteaux (1988), Comparative evolution of the Senegal

595 and eastern central Atlantic basins, from mineralogical and geochemical investigations,

596 *Sedimentology*, *35*, 85-103.

597 Chevillotte, V., D. Chardon, A. Beauvais, P. Maurizot, and F. Colin (2006), Long-term

598 tropical morphogenesis of New Caledonia (Sothwest Pacific): importance of positive

599 epirogeny and climate change, *Geomorphology*, *81*, 361-375.

600 Chukhrov, F.V., L.L. Shanin, and L.P. Yermilov (1966), Feasibility of absolute-age

601 determination for potassium-carrying manganese minerals, *Int. Geol. Rev.*, *8*, 278-280.

602 Colin, F., A. Beauvais, G. Ruffet, and O. Hénocque (2005), First ^{40}Ar/^{39}Ar geochronology of

603 lateritic manganiferous pisolites: Implications for the palaeogene history of a West African

604 landscape, *Earth Planet. Sci. Letters*, *238*, 172-188.

605 Collins, D.N., A.R. Tron, J.C. Wilson, and P. Parsonage (1971), The treatment of Tambao

606 Manganese Ore deposit for United Nations, *Unpublished report*, 24pp., Warren Spring

607 Laboratory, Department of trade and industry, CR504.

608 Dasgupta, S., S. Roy, and M. Fukuoka (1992), Depositional models for manganese oxides

609 and carbonates deposits of the Precambrian Sausar group, India, *Econ. Geol.*, *87*(5), 1412-

610 1418.

611 Delfour, J. (1963), Géologie du gîte de manganese de Tambao (haute-Volta), *Unpublished*

612 *BRGM report 5612*, 20 pp., BRGM, Orléans, France.

613   Faure, H. (1966), Reconnaissance géologique des formations sédimentaires post-

614   paléozoïques du Niger oriental, Doct sci. Thesis, Univ. Paris, Mém. B.R.G.M., 47,

615   Orléans, France.

616   Flower, B.P., and J.P. Kennett (1994), The middle Miocene climatic transition: East

617   antarctic ice sheet development, deep ocean circulation and global carbon cycling, *Science*,

618   *108*(3/4), 537-555.

619   Gavaud, M. (1977), Les grands traits de la pédogenèse au Niger méridional, Travaux et

620   Documents ORSTOM, 76, 104 pp., Paris, France.

621   Grandin, G. (1976), Aplanissements cuirassés et enrichissement des gisements de

622   manganèse dans quelques régions d'Afrique de l'Ouest, Doct sci. thesis, Univ. Strasbourg,

623   Mém. ORSTOM, 82, Paris, France.

624   Gunnell, Y. (2003), radiometric ages of laterites and constraints on long-term denudation

625   rates in West Africa, *Geology*, *31*(2), 131-134.

626   Hall, C.M., R.C. Walter, J.A. Westgate, and D. York (1984), Geochronology, stratigraphy

627   and geochemistry of Cindery tuff in Pliocene hominid-bearing sediments of the middle

628   Awash, Ethiopia, *Nature*, *308*, 26-31.

629   Hautmann, S., and H.J. Lippolt (2000), ^{40}Ar/^{39}Ar dating of central European K-Mn oxides a

630   chronological framework of supergene alteration processes during the Neogene, *Chem.*

631   *Geol.*, *170*(1-4), 37-80.

632   Hénocque, O., G. Ruffet, F. Colin, and G. Féraud (1998), ^{40}Ar/^{39}Ar dating of West African

633   lateritic cryptomelanes, *Geochim. Cosmochim. Acta*, *62*(16), 2739-2756.

634   Kennett, J.P., and N.J. Shackleton (1976), Oxygen isotopic evidence for the development of

635   the psychrosphere 38 Ma ago, *Science*, *260*, 513-515.

636   King, L.C. (1967), *The morphology of the Earth. A study and synthesis of world scenery*,

637   2nd ed., Olivier & Boyd, Edinburgh, Scottland.

638 Lang, J., C. Kogbe, S. Alidou, K. A. Alzouma, G. Bellion, D. Dubois, A. Durand, R.

639   Guiraud, A. Houessou, I. de Klasz, E. Romann, M. Salard-Cheboldaeff, and J. Trichet

640   (1990), The continental terminal of West Africa, *J. Afr. Earth Sci.*, *10*(1-2), 79-99.

641 Lawver, L.A., L.M. Gahagan, and M.F. Coffin (1992), The development of paleoseaways

642   around Antarctica, in *The Antarctic Paleoenvironment: A perspective on global change*,

643   edited by L.P. Kennett and D.A. Warnke, pp. 7-30, Antarctic Research Series, 56.

644 Lippolt, H.J., and S. Hautmann (1995), $^{40}Ar/^{39}Ar$ ages of Precambrian manganese ore

645   minerals from Sweden, India and Morocco, *Miner. Deposita*, *30*, 246-256.

646 Ly, A. (1985), Le Tertiaire de Casamance (Sénégal) : Biostratigraphie (Foraminifères) et

647   sédimentologie d'après les données de subsurface, Doct. sci. Thesis, 215 pp., Univ. Aix-

648   Marseille III, Marseille, France.

649 Ly, A., and R. Anglada (1991), Le Bassin Sénégalo-Mauritanien dans l'évolution des marges

650   périatlantiques au Tertiaire, *Cahiers de Micropaléontologie*, *6*, 2, 23- 40.

651 Michel, P. (1973), Les Bassins des fleuves Sénégal et Gambie : étude géomorphologique,

652   Doct sci. Thesis, Univ. Strasbourg, Mém. ORSTOM, 63, Paris, France.

653   Michel, P. (1978), Cuirasses bauxitiques et ferrugineuses d'Afrique Occidentale Aperçu

654   chronologique, *Trav. Doc. Géogr. Trop.*, *33*, pp. 11-32, CEGET CNRS, Bordeaux, France.

655 Miller, K. G., M. A. Kominz, J. V. Browning, J. D. Wright, G. S. Mountain, M. E. Katz, P.

656   J. Sugaman, B. S. Cramer, N. Christie-Blick, and S. F. Pekar (2005), The phanerozoic

657   record of global sea-level change, *Science*, *310*, 1293-1298.

658 Millot, G. (1970), *Geology of clays*, Chapman and Hall, London.

659 Millot, G. (1983), Planation of continents by intertropical weathering and pedogenetic

660   processes, in *lateritisation processes*, pp. 53-63, edited by A. J. Melfi and A. Carvalho,

661   Proceedings of the IInd international Seminar on Lateritisation Processes, Sao Paulo, Brazil.

662 Nahon, D. (1991), *Introduction to the petrology of soils and chemical weathering*, John

663   Wiley and sons, New York.

664 Nahon, D., A. Beauvais, P. Nziengui-Mapangou, and J. Ducloux (1984), Chemical

665   weathering of Mn-garnets under lateritic conditions in northwest Ivory Coast (West

666   Africa), *Chem. Geol.*, *45*, 53-71.

667 Nahon, D., B. Boulangé, and F. Colin (1992), Metallogeny of weathering: an introduction, in

668   *Weathering, soils & paleosols*, pp. 445-467, edited by I.P. Martini and W. Chesworth,

669   Developments in Earth Surface Processes 2, Elsevier, Amsterdam.

670 Oswald, J. (1992), Genesis and paragenesis of the tretravalent manganese oxides of the

671   australian continent, *Econ. Geol.*, *87*(5), 1237-1253.

672 Parc S., D. Nahon, Y. Tardy, and P. Vieillard (1989), Estimated solubility products and field

673   of stability for cryptomelane, nsutite, birnessite and lithiophorite based on natural lateritic

674   weathering sequences, *Amer. Miner.*, *74*, 466-475.

675 Partridge, T.C., and R.R. Maud (1987), Geomorphic evolution of Southern Africa since the

676   Mesozoic, *S. Afr. J. Geol.*, *90*, 179-208.

677 Pedro, G. (1968), Distribution des principaux types d'altération chimique à la surface du

678   globe, *Rev. Géogr. Phys. Géol. Dyn.*, *10*(5), 457-470.

679 Perseil E.A., and G. Grandin (1978), Evolution minéralogique du manganèse dans trois

680   gisements d'Afrique de l'Ouest : Mokta, Tambao, Nsuta. *Miner. Deposita*, *13*, 295-311.

681 Petters S.W. (1977), Ancient Seaway across the Sahara, *Nigerian Field*, *42*, 23-31.

682 Picot P., and R. Trinquard (1969), La manganosite (MnO) du gîte de manganèse de Tambao

683   (Haute-Volta), *Bull. Soc. fr. Minér. Cristallogr.*, *92*, 500-502.

684 Pracejus B., and B.R. Bolton (1992), Geochemistry of supergene manganese oxide deposits,

685   Groote Eylandt, Australia, *Econ. Geol.*, *87*(5), 1310-1335.

686   Retallack G.J., J.G Wynn, and T.J. Fremd (2004), Glacial-interglacial-scale paleoclimatic

687   change without large ice sheets in the Oligocene of central Oregon, *Geology*, 32(4), 297-

688   300.

689   Roddick J. C. (1983), High precision intercalibration of ^{40}Ar/^{39}Ar standards. *Geochim.*

690   *Cosmochim. Acta*, *47*, 887-898.

691   Roy S. (1981), *Manganese deposits*, Academic press, London.

692   Roy S. (1988), Manganese metallogenesis : a review, *Ore Geol. Rev.*, *4*(1-2), 155-170.

693   Ruffet G., C. Innocent, A. Michard, G. Féraud, A. Beauvais, D. Nahon, and B. Hamelin

694   (1996), A geochronological ^{40}Ar/^{39}Ar and ^{87}Rb/^{87}Sr study of K-Mn oxides from the

695   weathering sequence of Azul (Brazil), *Geochim. Cosmochim. Acta*, *60*, 2219-2232.

696   Salamy K.A., and J.C. Zachos (1999), Latest Eocene-Early Oligocene climate change and

697   Southern Ocean fertility : inferences from sediment accumulation and stable isotope data,

698   *Pal. Pal. Pal.*, *145*, 61-77.

699   Segev A., L. Halicz, B. Lang, and G. Steinitz (1991), K-Ar dating of manganese minerals

700   from the Eisenbach region, Black Forest, Southwest Germany, *Schweiz. Mineral. Petrogr.*

701   *Mitt.*, *71*, 101-114.

702   Tardy Y., and C. Roquin (1998), *Dérive des continents, paléoclimays et altérations*

703   *tropicales*, BRGM, Orléans, France.

704   Thomas, M.F. (1994), *Geomoprhology in the tropics. A study of weathering and denudation*

705   *in low latitudes*, Wiley, New York.

706   Turner G. (1971), ^{40}Ar-^{39}Ar ages from the lunar maria, *Earth Planet. Sci. Lett.*, *11*, 169-191.

707   Turner G., and P.H. Cadogan (1974). Possible effects of ^{39}Ar recoil in ^{40}Ar-^{39}Ar dating, paper

708   presented at 5th lunar Conference, 2, 1601-1615.

709   Turner S., and P.R. Buseck (1979), Manganese Oxide Tunnel Structures and their

710   Intergrowths, *Science*, *203*, 456-458.

711 Varentsov I.M., and D.I. Golovin (1987), Groote Eylandt Manganese deposit, North

712   Australia : K-Ar age of cryptomelane ores and aspects of genesis, *Reports Acad. Sci.*

713   USSR, 294(1), 203-207.

714 Varentsov I.M. (1996), *Manganese ores of supergene zone : geochemistry of formation*,

715   Kluwer Academic Publisher, Dordrecht, The Netherlands.

716 Vasconcelos P.M. (1999), K-Ar and $^{40}Ar/^{39}Ar$ geochronology of weathering processes, *Annu.*

717   *Rev. Earth Planet. Sci.*, *27*, 183-229.

718 Vasconcelos P.M., T.A. Becker, P.R. Renne, and G.H. Brimhall (1992), Age and duration of

719   weathering by ^{40}K-^{40}Ar and $^{40}Ar/^{39}Ar$ analysis of Potassium-Manganese Oxides, *Science*,

720   *58*, 451-455.

721 Vasconcelos P.M., P.R. Renne, T.A. Becker, and H.R. Wenk (1995), Mechanisms and

722   kinetics of atmospheric, radiogenic, and nucleogenic argon release from cryptomelane

723   during $^{40}Ar/^{39}Ar$ analysis, *Geochim. Cosmochim. Acta*, *59*(10), 2057-2070.

724 Vasconcelos P.M., P.R. Renne, G.H. Brimhall, and T.A. Becker (1994), Direct dating of

725   weathering phenomena by $^{40}Ar/^{39}Ar$ and K-Ar analysis of supergene K-Mn oxides,

726   *Geochim. Cosmochim. Acta*, *58*, 1635-1665.

727 Vogt, J. (1959), Aspects de l'évolution géomorphologique récente de l'Ouest africain, *Ann.*

728   *Géogr. Fr.*, *68*(367), 193-206.

729 Yashvili L.P., and R.K. Gukasyan (1974), Use of cryptomelane for potassium-argon dating

730   of manganese ore of the Sevkar-Sargyukh deposit, Armenia, *Doklady Earth Sci. Sect.*, *212*,

731   49-51.

732 Zachos J.C., M. Pagani, L. Sloan, E. Thomas, and K. Billups (2001), Trends, rhythms, and

733   aberrations in global climate 65 Ma to present, *Science*, 292, 686-693.

734   Zachos J.C., T.M. Quinn, and K.A. Salamy (1996), High-resolution (104 years) deep-sea

735   foraminiferal stable isotope records of the Eocene-Oligocene climate transition,

736   *Paleoceanography*, *11*(3), 251-266.

737   Zachos J.C., L.D. Stott, and K.C. Lohmann (1994), Evolution of early Cenozoïque marine

738   temperatures, *Paleoceanography*, *9*(2), 353-387.

739   Zartman R. E. (1964), A geochronological study of the Love Grove Pluton from the Llano

740   uplift, Texas, *Journal of Petrology*, *5*, 359-408.

741

Figures caption

Figure 1. Synthetic geomorphological sequence of lateritic paleolandsurfaces in West Africa

(The rectangle defines the Tambao sequence in North Burkina Faso).

Figure 2. Location and geomorphologic patterns of the Mn-ore deposit of Tambao in North

Burkina Faso, with the locations of the drill cores, and a section (A-B) across the main

geological formations (blue circle in the inset = intracratonic sedimentary basin).

Figure 3. Logs of the drill cores with the locations of samples dated by the ^{39}Ar-^{40}Ar method.

Figure 4. (a) SEM photomicrograph of cryptomelane needles with (b) its chemical analysis.

Figure 5. Photomicrographs of (a) cryptomelane (C) vein, (b) cryptomelane (C) developing

from the metasomatism of pyrolusiste (P), and (c) botryoidal cryptomelane.

Figure 6. Geochemical evolution along DD2B drill core.

Figure 7. ^{39}Ar-^{40}Ar age spectra configuration, (a) Type 1 (stair case), (b) Type 2 (hump) shape

and (c) Type 3. (ca. = concordant apparent ages)

Figure 8. ^{39}Ar-^{40}Ar age spectra of cyptomelane extracted from the upper part of the deposit

(342-325 m altitudes), (a) outcrop and intermediate surface samples, (b) DDH76-02 drill

core, (c) DD2B drill core, and (d) frequency diagram of apparent ages. (See figure 3 for

sample locations).

Figure 9. ^{39}Ar-^{40}Ar age spectra of cyptomelane extracted from the upper and middle parts of

the deposit (325-300 m altitudes), (a) outcrop samples, (b) and (c) DD2B drill core, (d)

DDH76-02 drill core, (e) and (f) DDH76-09 drill core, and (g) frequency diagram of

apparent ages. (See figure 3 for sample locations).

771   Figure 10. ^{39}Ar-^{40}Ar age spectra of cyptomelane extracted from the lower part of the deposit

772   (300-253 altitudes), (a) samples from DD2B, DDH76-09 drill cores and low glacis (b)

773   DDH76-02 drill core, and (c) frequency diagram of apparent ages. (See figure 3 for sample

774   locations).

775
776   Figure 11. (a) Distribution of pseudo-plateau and plateau ages as a function of altitude in the

777   Mn-deposit with the superimposition of the elevation ranges of each landsurface (b) 3D

778   frequency diagram of all apparent ages versus altitude. (Curved black arrow = decreasing

779   chemical weathering and increasing erosion rate).

780
781   Figure 12. Comparison between the global curves of (a) δ^{18}O-paleotemperatures and (b)

782   eustatic levels, both from *Miller et al.* [2005], with (c) ^{39}Ar-^{40}Ar age groups (grey scale

783   bands) defined by pseudo-plateau or plateau ages depicted in this work. (The dotted grey

784   curve in (b) is the long term fit of the sea level curve and the straight dotted black segments

785   represent the erosion periods; the rectangle and dotted rectangles in (c) represents the ^{39}Ar-

786   ^{40}Ar age groups previously obtained by *Henocque et al.* [1998] and *Colin et al.* [2005],

787   respectively; the dark grey histogram in (c) represents the age frequency weighted by the

788   error margin for the deposit as a whole; the light grey scale band represents the paroxysm of

789   the bauxitic weathering period).

790
791   Figure 13. (a) Geomorphological relationships between the lateritic paleolandsurfaces (dotted

792   lines) and the sedimentary sequences of the Iullemmeden basin of Niger in West Africa (the

793   light grey trapezoids represent the denuded bauxites and the vertical black arrow represents

794   the total denudation of the regolith. (b) Detailed morphogenetic processes around Tambao

795   (black numbers = weathering periods in Ma; grey numbers = erosion periods in Ma; vertical

796   grey arrows = regolith denudation and topographic decay).

797

797

798

799
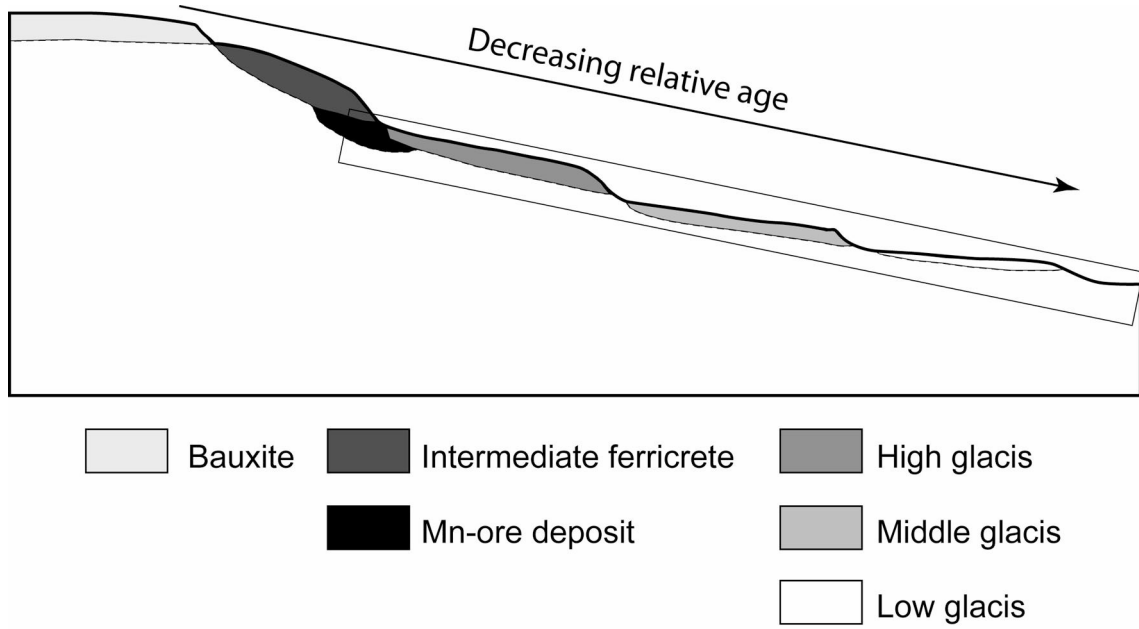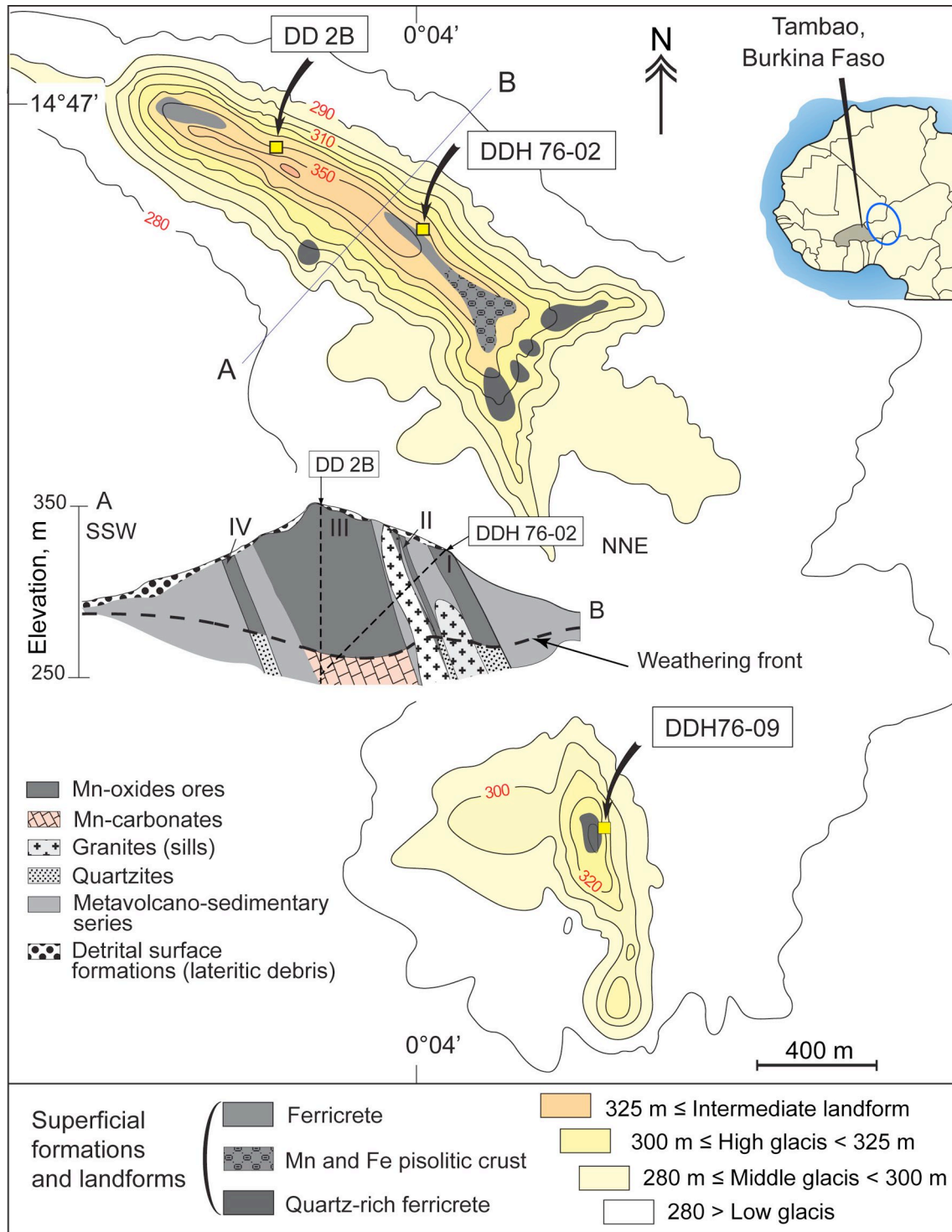
Decreasing relative age

	Bauxite		Intermediate ferricrete		High glacis
	Mn-ore deposit		Middle glacis
					Low glacis

Fig. 1

Beauvais et al., 2008

800

801

801

Fig. 2

802

803

803

804

805

High hill

Low hill

Elevation, m

BF96-108
BF96-107

BF96-104
BF96-102
BF96-101
BF96-98
BF96-97

BF96-96

BF96-94

BF96-273

BF96-299

BF96-314
BF96-318
BF96-322
BF96-327

DDH76-02

I

II

III

IV

BF96-202

BF96-211
BF96-215

BF96-218

BF96-229

BF96-251
BF96-256
BF96-260

BF96-93

BF96-91

BF96-62

BF96-559
BF96-561
BF96-563

BF96-571

BF96-575
BF96-577

BF96-581

DDH76-09

DD-2B

Detrital lateritic material
Mn-oxides ore
Weathered granite
Kaolinite
Weathered schist
Mn-Carbonate
Albitite sill
Granite sill
Core loss
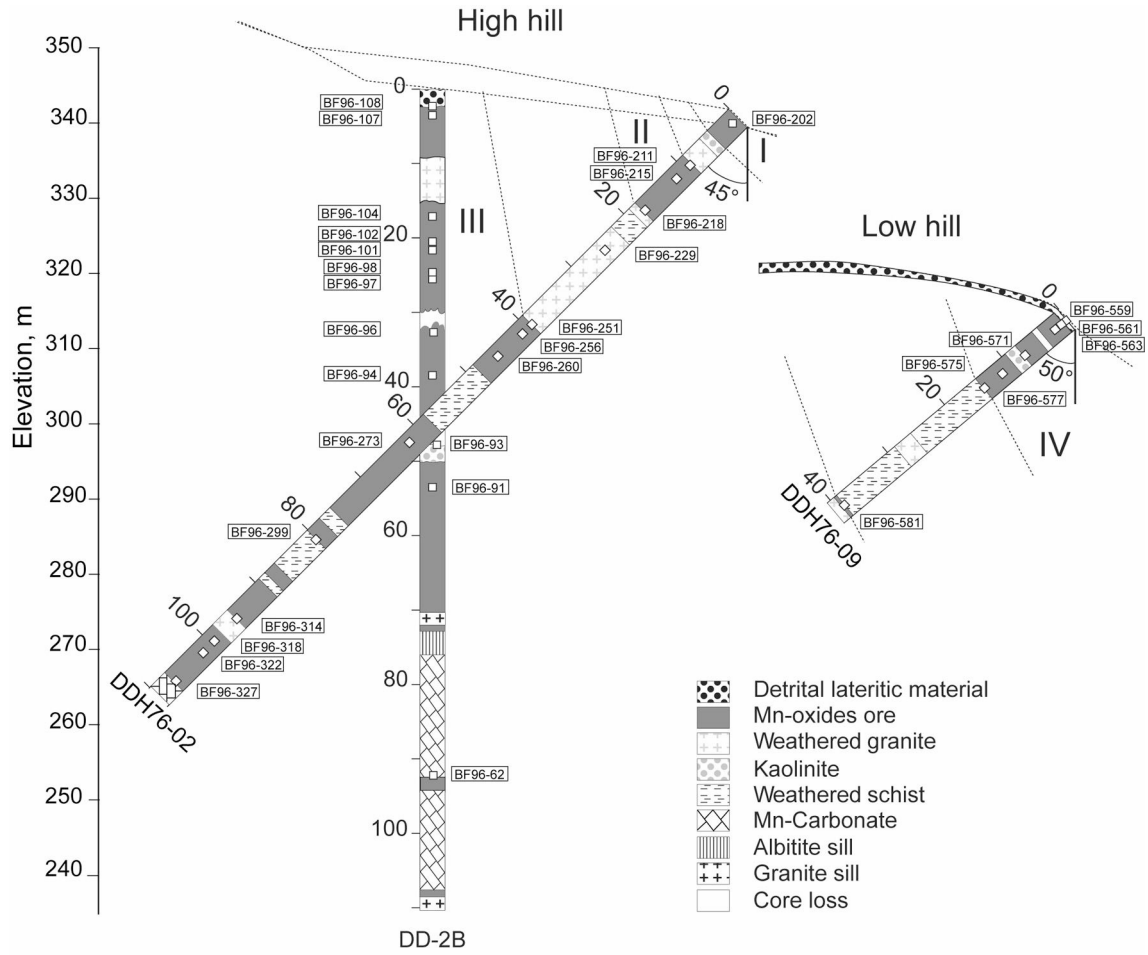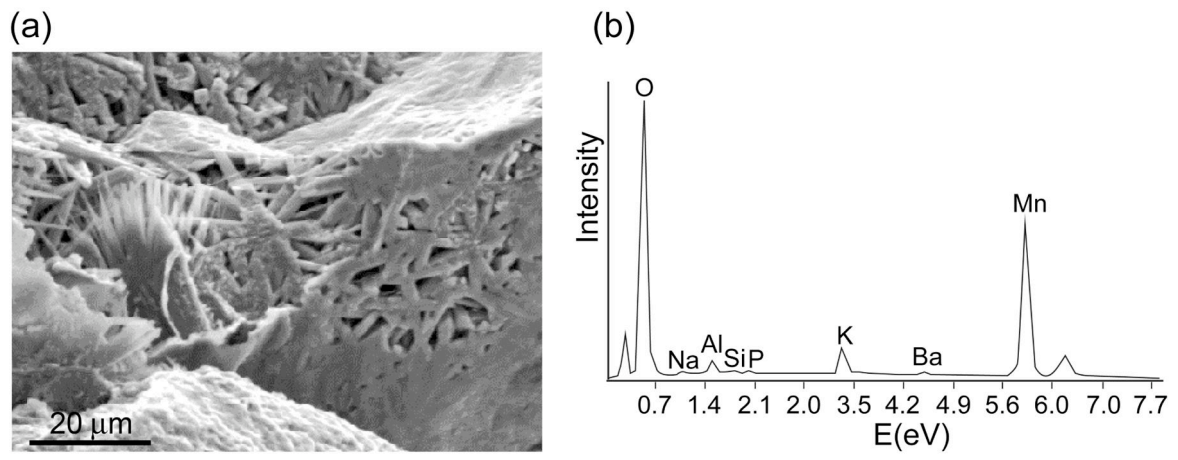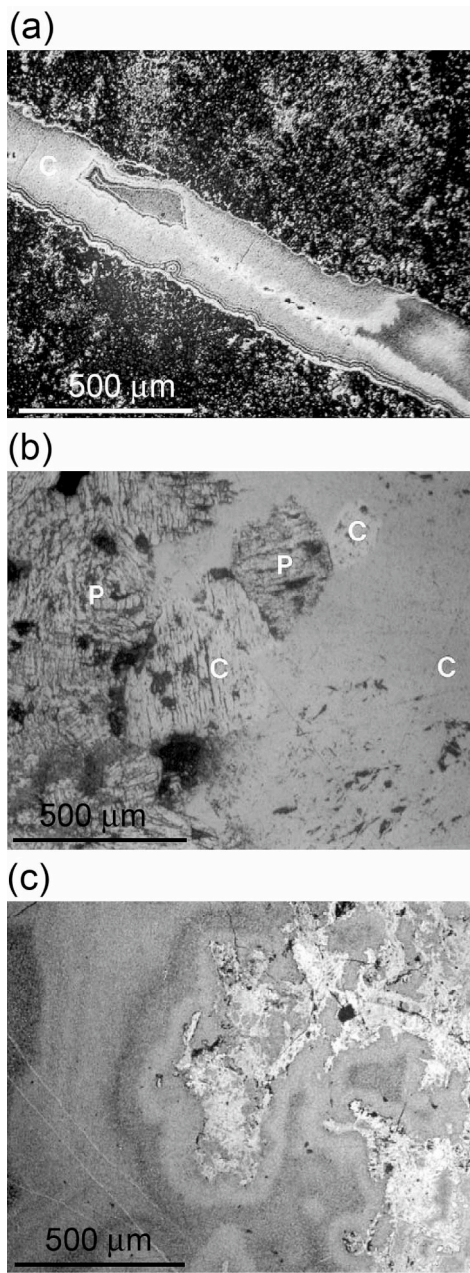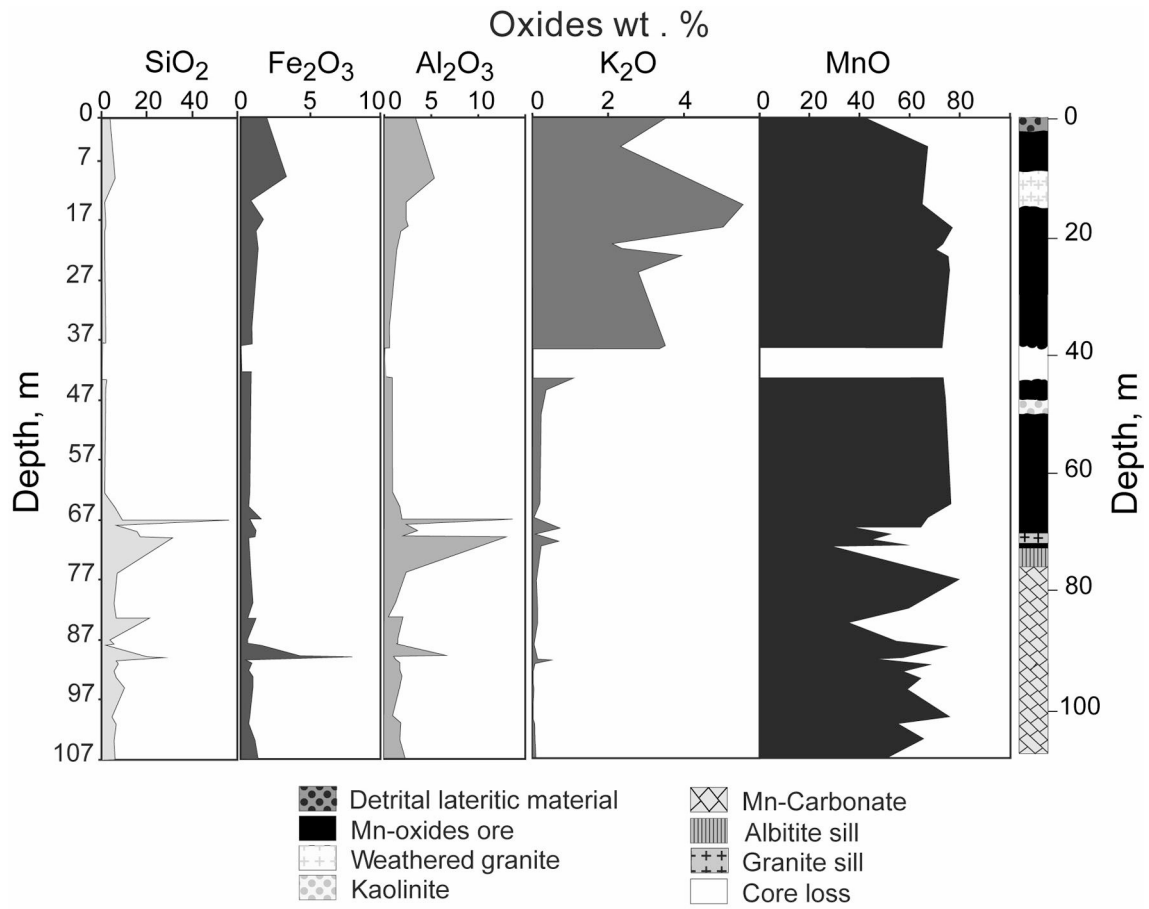
Fig.3

Beauvais et al., 2008

806

807

807

808

(a)

(b)

Fig. 4   *Beauvais et al., 2008*

809

810

812

Fig. 6

Beauvais et al., 2008

813

814

814
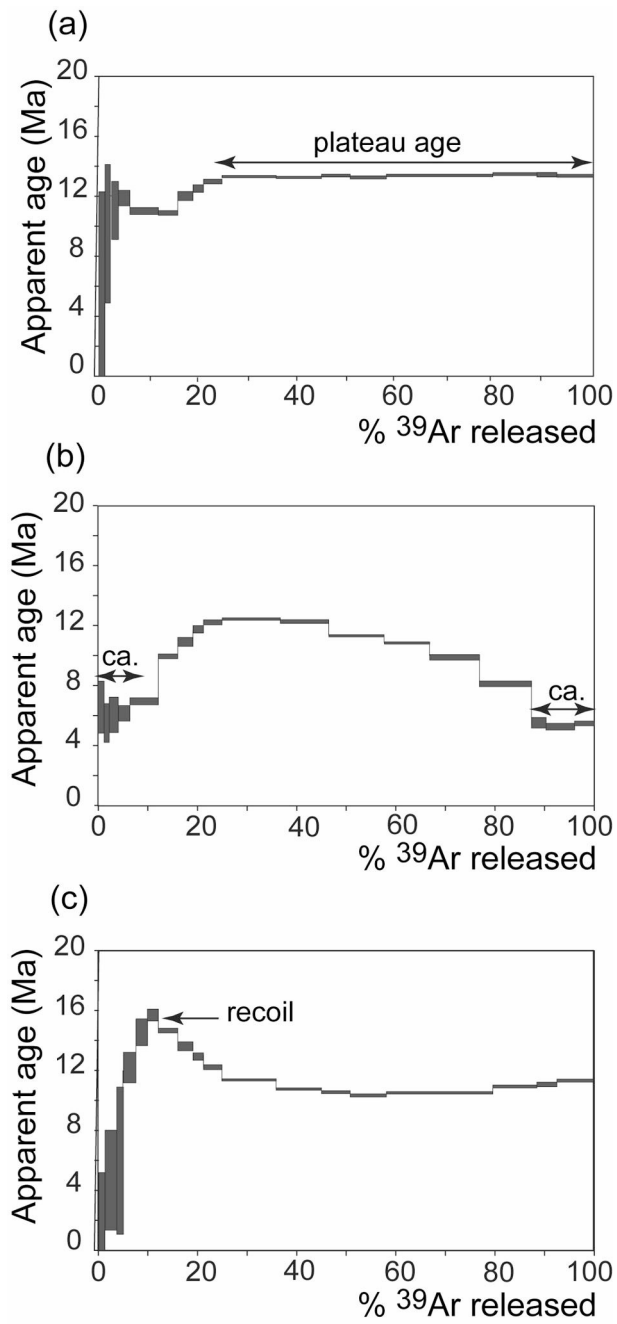
Fig. 7

Beauvais et al., 2008

815

816

816

817

818

Figure 8

819

820
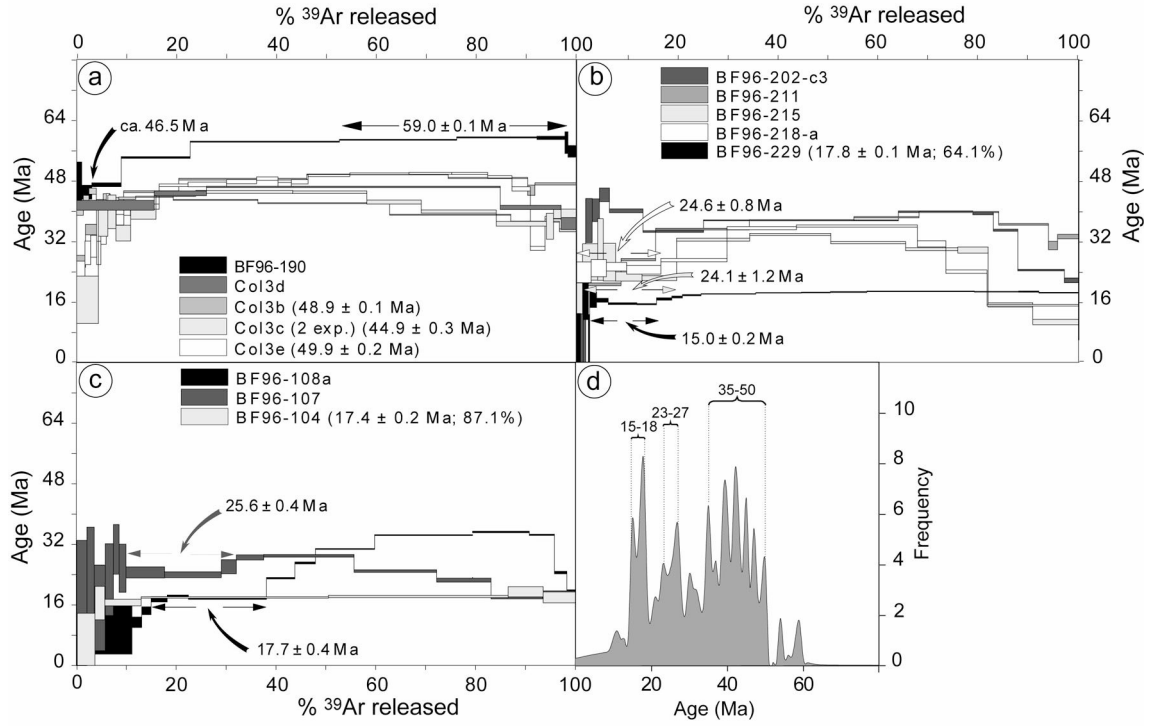
Figure 9
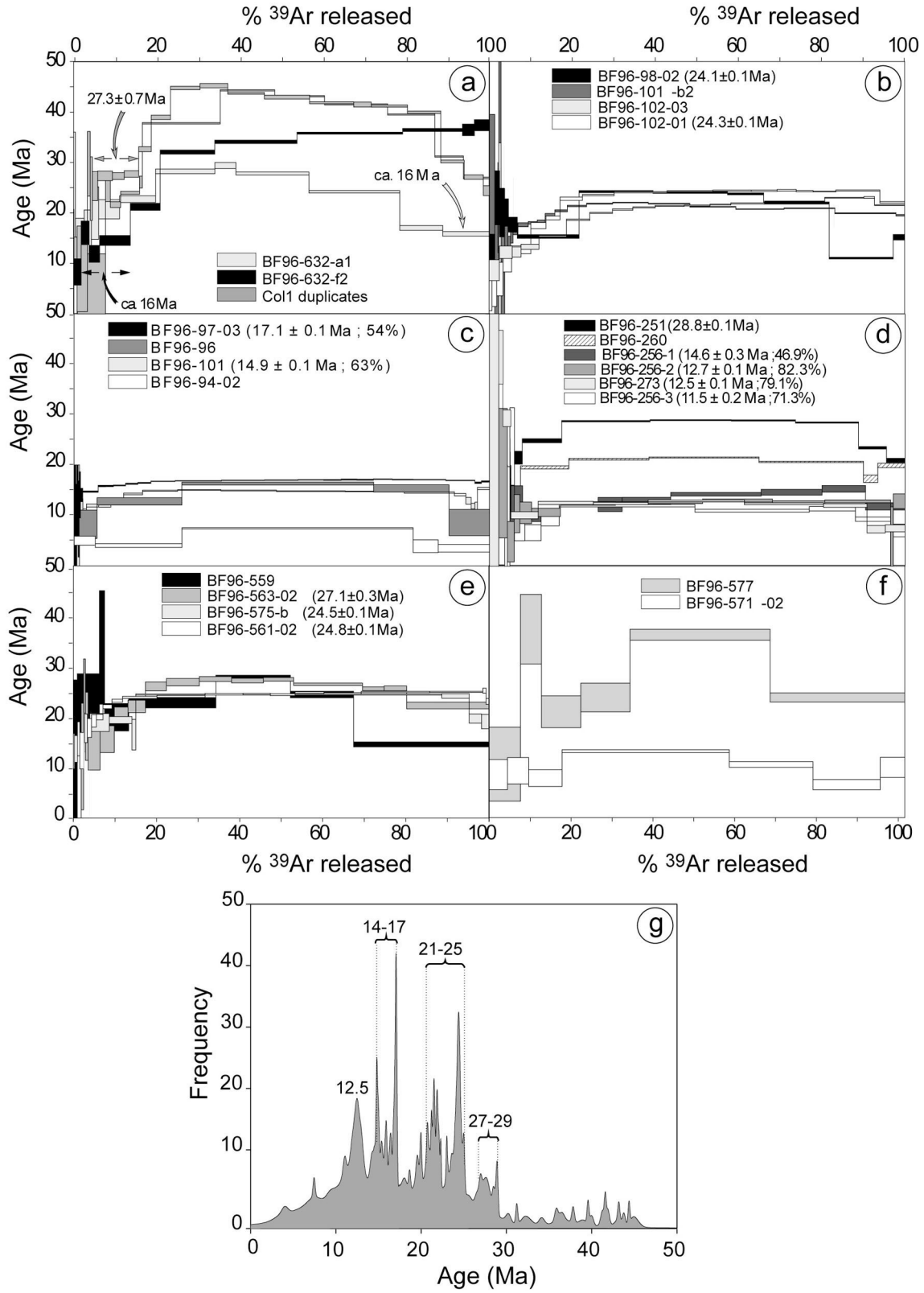
Beauvais et al., 2008

821

822

823

Figure 10

824

825

825

FIG. 11

826
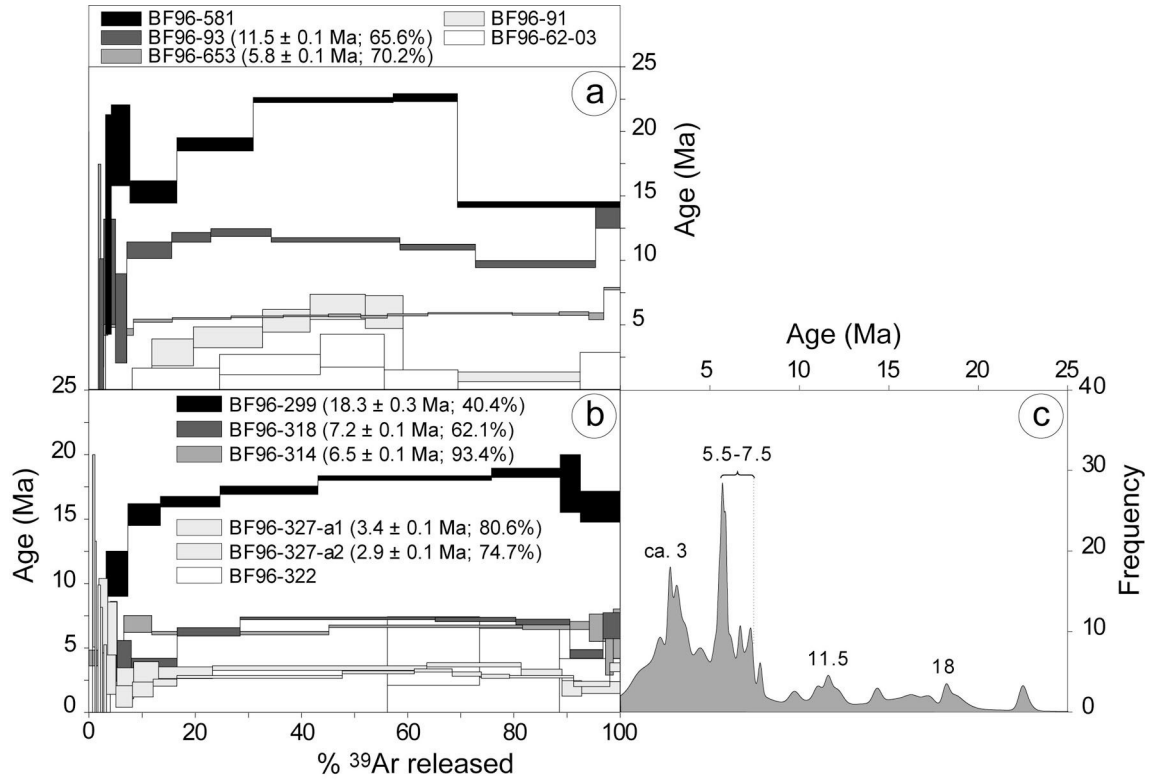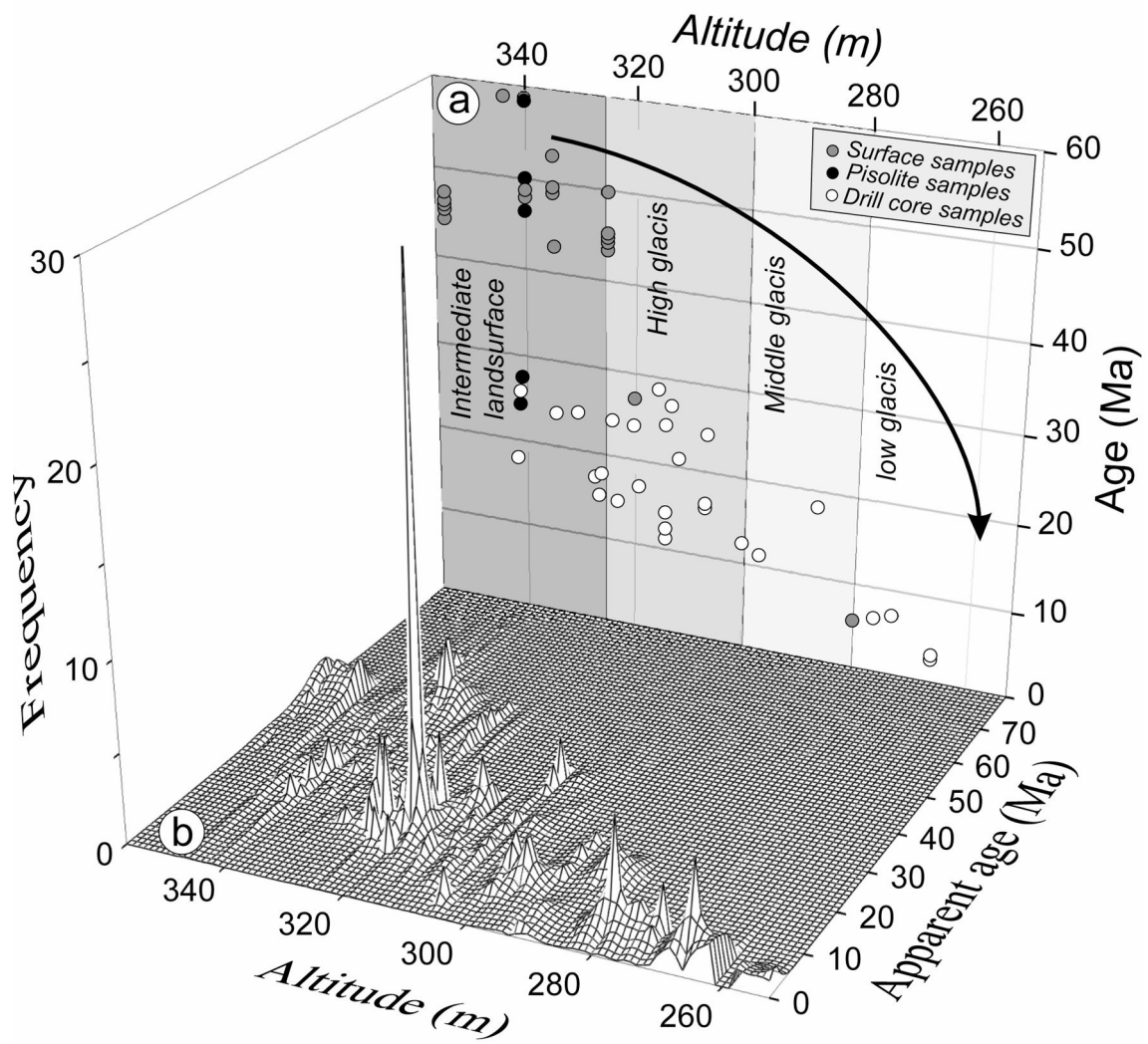
827

827
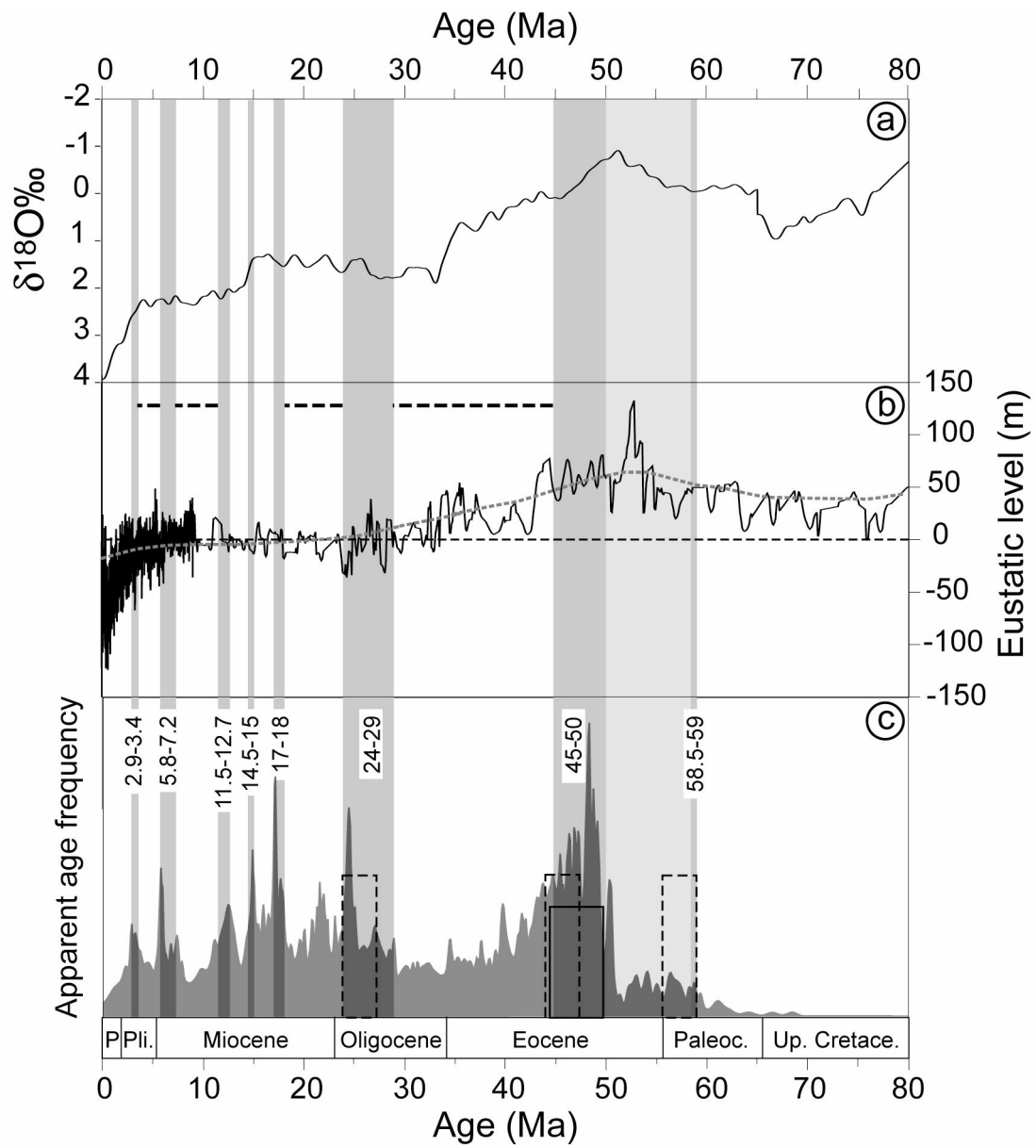
FIG. 12

Beauvais et al., 2008

828

829

829

830

Figure 13

831